Mitigation of ionospheric signatures in Swarm GPS gravity field estimation using weighting strategies

Lucas Schreiter[1], Daniel Arnold[1], Veerle Sterken[1], and Adrian Jäggi[1]

[1]Astronomical Institute, University of Bern, Sidlerstrasse 5, 3001 Bern, Switzerland

Correspondence: Lucas Schreiter (lucas.schreiter@aiub.unibe.ch)

Abstract. Even though ESA's three-satellite mission Swarm is primarily a magnetic field mission, it became more and more important as gravity field mission. Located in a low earth orbit with altitudes of $460km$ for Swarm A and Swarm C and $530km$ for Swarm B, after the commissioning phase, and equipped with geodetic-type dual frequency GPS receivers, it is suitable for gravity field computation. Of course the Swarm GPS-only gravity fields are not as good as the gravity fields derived from

5   the ultra precise GRACE K-Band measurements, but due to the end of the GRACE mission in October 2017, data gaps in the previous months, and the gap between GRACE and the recently launched GRACE Follow-On mission, Swarm gravity fields became important to maintain a continuous time series and bridge the gap. By validating the Swarm gravity fields to the GRACE gravity fields, systematic errors have been observed, especially around the geomagnetic equator. These errors are already visible in the kinematic positioning from where they propagate into the gravity field solutions.

10   We investigate these systematic errors by analyzing the geometry-free linear combination of the GPS carrier phase observations. Based on this we present different weighting schemes and investigate their impact on the gravity field solutions in order to assess the success of different mitigation strategies.

1   Introduction

15   Even though Swarm was designed as a magnetic field mission, Swarm became important as a gravity mission to bridge the gap between Grace and Grace Follow On (Lück et al., 2018). The GRACE K-Band gravity fields were ultra precise, but due to battery aging starting in 2011, they started having gaps and finally no more GRACE gravity fields were available since June 2017. The GRACE mission ended in October 2017. GRACE Follow On was launched on May 22, 2018, resulting in a gap of more than half a year.

20   Recent comparisons of GRACE (K-Band) gravity fields to Swarm (GPS-only) gravity fields showed two pronounced band shaped artifacts of about $4cm$ in geoid height along the geomagnetic equator, when adopting a gauss filter of $500km$ (Jäggi et al., 2016). A similar behavior of LEO based GPS-only gravity fields was observed earlier in the computation of GOCE GPS-only gravity fields (Jäggi et al., 2015). In the GOCE case only the ascending arcs ($\sim 18h$ magnetic local time(MLT)) showed

this behavior (Bock et al., 2014). This special MLT is well-known for a very pronounced equatorial ionization anomaly, equatorial spread F, as well as equatorial plasma bubbles (Whalen (2000), Stolle et al. (2006)). In this region high gradients exist in the plasma density, which in turn may affect the tracking.

Usually for the kinematic positioning the ionosphere-free linear combination

$$L_{IF} = \frac{1}{f_1^2 - f_2^2} \cdot (f_1^2 L_1 - f_2^2 L_2) \tag{1}$$

is used, where f_1 and f_2 are the carrier frequencies and L_1 and L_2 are the two phase observables. By this first order terms of the ionospheric phase advance cancels out. The remaining parts tend to be very small and were found to be negligible for the presented investigation (Jäggi et al., 2015).

The differences between the Swarm and GRACE gravity fields significantly improved with the tacking loop updates of the GPS

10 receivers performed by ESA (Dahle et al., 2017), which is an indicator, that the high ionospheric activity affects the receiver tracking and in turn contaminates the ionosphere-free linear combination.

In contrast to the sun-synchronous GOCE orbit, where only ascending arcs were affected due to the dusk-dawn orbit geometry (Jäggi et al., 2011a), the Swarm orbit is evolving in MLT, and a separation in ascending and descending arcs would therefore not fix the local time. Therefore we prefer to use ionospheric information, directly derived from the GPS measurements. Such

15 an approach was already successfully used by Jäggi et al. (2016) using epoch differences (a numerical first time derivative) of the geometry-free linear combination

$$L_{GF} = L_1 - L_2. \tag{2}$$

In case the absolute value of the derivative exceeded $0.02 m/s$ the GPS observations were rejected. Even though it successfully removed most of the signatures, the orbit was weakened due to the increased number of ambiguity parameters caused by gaps

20 around the geomagnetic equator, as we will show later. In this article we present a refined approach by using weighting strategies and assess if higher order time derivatives may be an even more adequate criterium.

2 Systematic errors in kinematic positioning

2.1 Systematic errors in kinematic positioning

25 It was shown in earlier studies ((Jäggi et al., 2016), (Dahle et al., 2017)) that the artifacts in the gravity field solutions are caused by the ionosphere. For that reason we link excursions in the kinematic positions to the ambient plasma density. Swarm is eqipped with a Langmuir probes to directly measure in-situ plasma density. Figure 1 shows a comparison between the the measured plasma density and differences of kinematic positions to a reduced dynamic orbit, offering more dynamical stiffness. Especially around the sharp peak in plasma density jumps of up to four centimeters are observed in the orbit differences. If one

30 compares this to the ionosphere-free GPS phase residuals at the respective epochs, see figure 2(top), their epoch wise variance is getting larger (widening), indicating a inconsistency in the phase observables. The receiver clock is estimated such that the
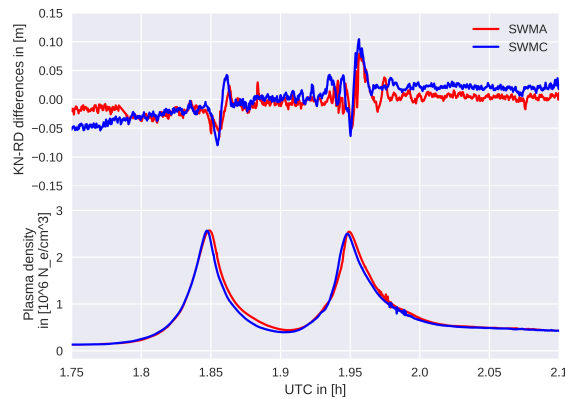
Figure 1. Orbit differences in the radial component between kinematic positions (KN) and a reduced-dynamic (RD) orbit fit (top) and plasma density during an equatorial pass.

epoch wise mean of the phase residuals gets minimized. For that reason the ionosphere-free phase residuals are not independent for different GPS satellites.

The widening occurs at the same epochs, where the measured plasma density has its peaks (see figure 1 and 2 top curves). Because the GPS-receiver is moving with a large velocity (about 7.7km/s), large gradients in the plasma density are clearly

5   reflected in the geometry-free linear combination. Due to the different line-of-sights to the GPS-satellites, this geometry-free linear combination has a large variability.

In the following we establish criteria for the occurence of the widening in the ionosphere-free phase residuals. We use its numerical derivatives, because the widening seems to be associated with rapid changes in plasma density and thus in the geometry-free linear combination. The geometry-free linear combination can be computed directly from the RINEX file. No

10   additional information, e.g., an a priory orbit based on an underlying gravity field, is needed. The ionosphere-free phase residuals, as shown in figures 2 and 7, were computed by using a reduced dynamic orbit with 15 min piecewise constant accelerations. The same residuals were used to define the thresholds used in the following. For the orbit computations the Bernese GNSS software package V5.3 was used (Dach et al., 2015). In all cases a standard GPS phase screening was performed, rejecting large ionosphere-free phase residuals ($> 4cm$). This is consistent with the standard orbit processing at the Astronomical Institute of

15   the University of Bern (AIUB).

2.2   Kinematic covariances

The the covariance information may be used as an indicator for the quality of kinematic positions for gravity field processing. As shown by Jäggi et al. (2011b), however, this basically represents the geometry of the observation. If affected epochs have a high covariance they do not propagate into gravity field solutions, because they get properly weighted according to the covariance information. Because we saw, that the spikes are associated with a spreading of the Phase residuals, we compare
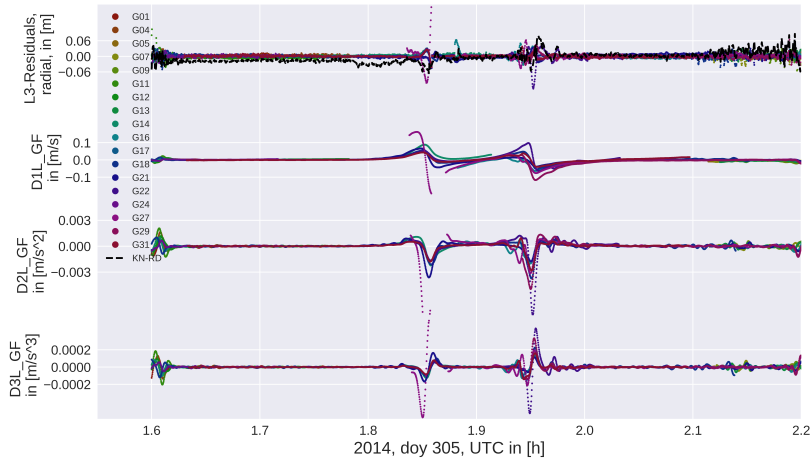
Figure 2. Phase residuals in kinematic positioning (top) and time derivatives of the geometry-free linear combination during one equatorial pass.

the kinematic covariance with the epoch wise standard deviation of the phase residuals, see figure 3. We use magnetic latitude and magnetic local time because the phenomena is most prominently visible around the magnetic equator in the evening hours. For the kinematic variances we used the formal error propagation in radial direction,

$$\sigma_r = (1/r^2) \cdot (x^2 \cdot k_{xx} + y^2 \cdot k_{yy} + z^2 \cdot k_{zz} + 2 \cdot x \cdot y \cdot k_{xy} + 2 \cdot x \cdot z \cdot k_{xz} + 2 \cdot y \cdot z \cdot k_{yz}),$$

where x, y and z are the coordinates in an earth fixed system and k_{xy} denotes the covariance between x, y and r is the radius. We use this to represent the quality of the 3D-positions in radial direction, whereas we used the standard deviation of the phase residuals at a certain epoch. These values were binned, the mean of each box was computed, and for the purpose of visibility the logarithm was used for the kinematic variances. Both pictures look very different especially around the polar regions, where

5   large phase residuals are more frequently observed. A different behavior can also be seen around the geomagnetic equator. In this region the high standard deviation in phase residuals is also affecting earlier local times, and in slightly different latitudes, than the high variances in kinematic positioning. For both plots the same months (analyzed test period: 2015: Jan., Mar.; 2016: Feb., Mar., Jun., Jul., Aug.) were used and only kinematic positions with a minimum redundancy of 5 GPS-satellites were used. No additional weighting or screening was performed.

10   As shown by Xiong et al. (2016), the loss of locks of the Swarm GPS receivers are highly correlated to bubble events. Whereas loss of lock corresponds to the worst case scenario, we saw in figure 3, that the kinematic variances also generally increase in the potential bubble regions, i.e. after sunset $(18 - 22$ MLT$)$ and near the geomagnetic equator. In this study we extend the investigations by checking the covariances of the unweighted and un-screened kinematic positions for Swarm for a long time span. As shown in the previous section, the phase residuals increase around the peaks in plasma density, indicating
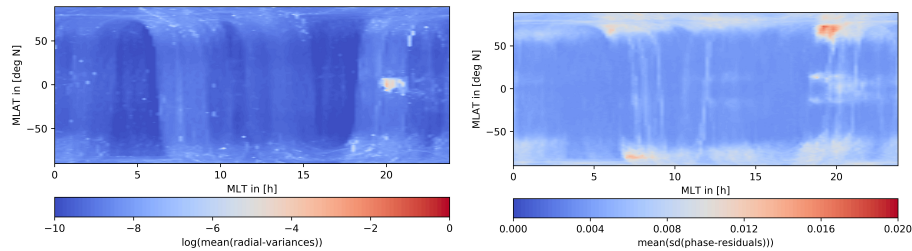
Figure 3. Kinematic variances (left) and spreading of phase residuals (right) binned in magnetic coordinates for the analyzed test period.
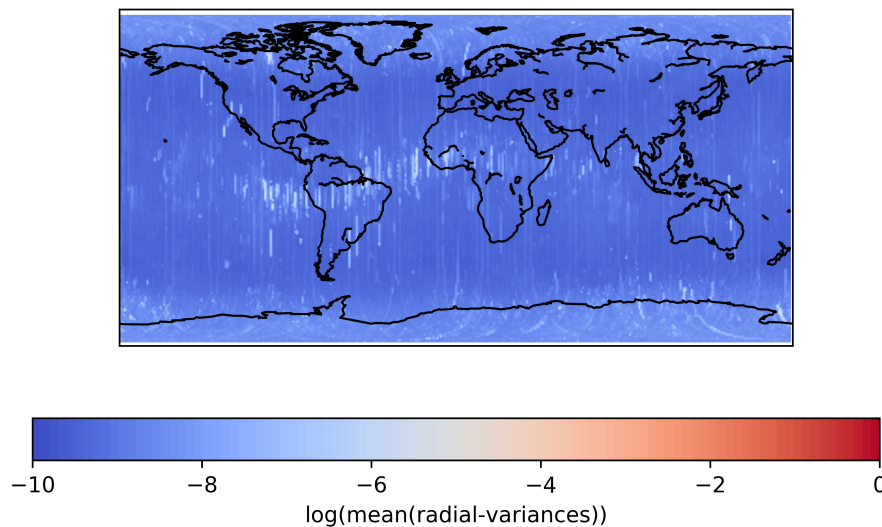
Figure 4. Kinematic covariances binned, Nov. 2013 - Dec. 2017

a potential degradation of the phase observables or a weaker geometry due to screened GPS-observations or possible loss of locks.

In figure 4 we binned the covariances in $1°lon \times 1°lat$ and formed the average using unweighted kinematic positions form $11/2013 - 12/2017$ and all three Swarm Satellites. Only positions with enough redundancy were used. Figure 4 shows that the geomagnetic equator is clearly visible showing the largest covariances. If one reproduces this plot in MLT and $Mlat$, compare figure 3 (left), a very pronounced peak around $18 - 22hMLT$ gets visible around $0Mlat$. It should be noted, that the time span used for figure 3 is by the analyzed test period and by this it is shorter than in figure 4. Nevertheless the observed patterns are almost identical to the results of Xiong et al. (2016), even if loss of locks or data gaps for all GPS-satellites are by construction not included in our figures. This again supports the statement, that the GPS data quality suffers from high activity in the magnetic-equatorial ionosphere at evening hours and, of course, due to equatorial plasma bubbles (see figure 3 (left)).
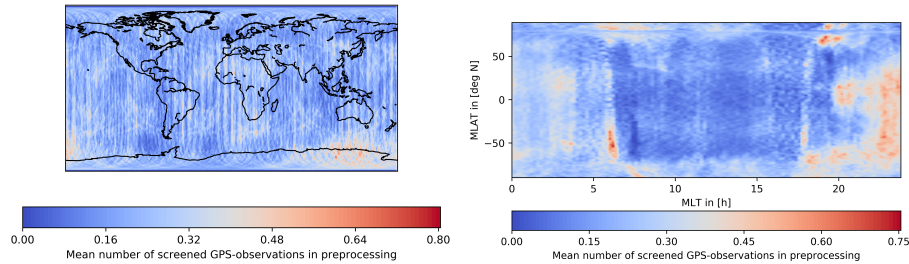
Figure 5. Average number of GPS-observations screened in the preprocessing for the analyzed test period.

2.3 Screened observations in preprocessing

In the standard orbit processing some observations are rejected in the preprocessing, because they are outliers, show large phase residuals, due to gaps, or small observation pieces. This screening is performed to avoid the propagation of data problems into the orbit solution. Even though this screening process applies especially in the night time hours, it does not seem to detect the observations responsible for the spikes in the kinematic positioning. The mean number of observations screened in the preprocessing is shown in figure 5. As before only valid kinematic positions with enough redundancy were used and the mean difference between the number of observations in the RINEX file and the observations used for the final kinematic positioning is shown.

2.4 Computation of derivatives

Due to the noise of the geometry-free linear combination the computation of meaningful derivatives is not straightforward. In order to obtain reliable derivatives we use a combination of a Gaussian filter and a Savitzky-Golay filter. First we smooth our data with the Gaussian filter, then we apply the Savitzky-Golay filter to obtain the next order derivative, we smooth again, etc.. This approach allows us to keep the windowsize and the degree for the Savitzky-Golay filter low and by this attenuate the sensitivity to noise in the higher order derivatives. Before applying the filters, we use a jump and outlier detection with a threshold of $0.5m/s$, applied on epoch differences of the geometry-free linear combination. If larger jumps occur, the arcs were split to avoid any contamination of the derivatives. This action was also performed if there were gaps of one or more epochs in the $1Hz$ RINEX data. For the Gaussian filter we select a bandwidth of $10s$, a symmetrical window with a total width of $10.1s$ and min. number points 10. For the Savitzky-Golay filter we choose a polynomial of degree 1, a symmetrical window with a total size of $12.5s$ and a min. number of points of 7. The parameters were determined empirically using an artificial signal (figure 6) and original Swarm RINEX data. Especially in case of the Gaussian Filter it is important to choose the parameters such that the window is almost full (with the mentioned setting: max. one epoch missing) and symmetrically occupied, otherwise we may bias the smoothed points to the mean of the previous ones, and pushing the derivatives to zero. If it was not possible to compute the derivative due to gaps or jumps, gaps or not enough data, the corresponding epochs were marked to handle them separately at a later stage. In our case we will downweight these epochs.
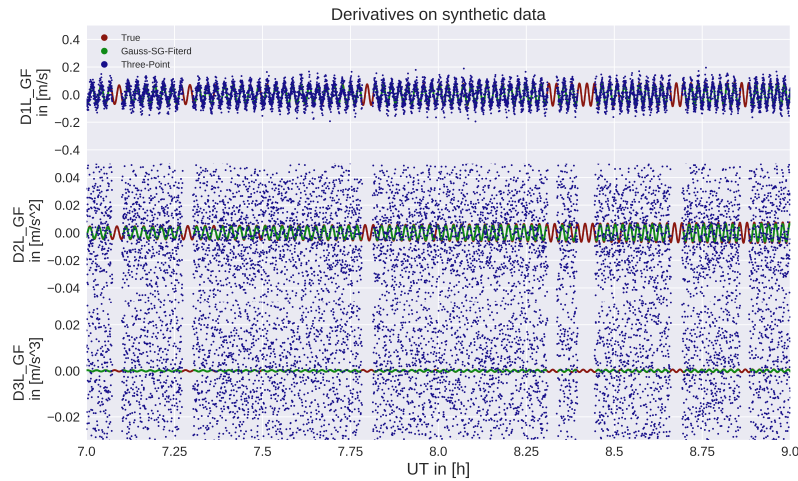
Figure 6. Tests on synthetic data. Red points indicates the true analytic noise-free derivative, green the computed derivatives from noisy data using the filter settings from section 2.4 and blue points the three point derivative scheme. The noise in the second and third plot visible in the blue points exceeds the limit of the axis

In Figure 2 we show a short time series of phase residuals and the corresponding derivatives during one equatorial pass. It may be seen that the second and third time derivative are more focused to the epochs where the spikes occure than the first time derivative. The higher derivatives show comparatively larger amplitudes at the boundaries, which correspond to the polar regions , indicating, that the quality of the derivatives might suffer from observation noise.

To check the consistency of the adopted differentiating schemes and to validate them, we simulated signal including random jumps, observation gaps and random noise. The Signal was simulated by $f(t) = \sin((100t)^2)$ where t is measured in days. A Gaussian noise with a standard deviation of $5cm$ was selected. The number of jumps and the number of gaps was set to 40 and the locations were determined randomly. The jump sizes are given by a Gaussian random variable with a standard deviation

10 of $5m$ and the length of gaps in seconds is determined by a Poisson random variable with $\lambda = 100$. The Signal was chosen to have different frequencies with time, allowing to evaluate the performance of the differentiating scheme with frequency. In Figure 6 we compare the following two cases. We compute the derivatives in the first case with an almost non smoothed differentiating scheme using no Gaussian filter and only three points for the Salvitzky-Golay filter, and with the parameters mentioned above. If the smoothing is too weak, as one can see in the three-point case, the derivatives are very noisy. With the

15 stronger smoothing one gets a dampening of the higher frequencies (approximately 10% ,15% 25% for the first,second and third derivative at $0.015Hz$) , but in total the derivatives obtained represents the true derivative, as may be seen in figure 6. The gaps in the derivatives are given by artificial gaps in the data, but were further enlarged due to the min. number of points restriction.

3 Weighting of Observations

3.1 AIUB standard screening

As a reference the AIUB standard screening, as published in (Jäggi et al., 2016) is used. It successfully removed the signatures, although the orbit quality was weakened and the number of ambiguities increased. Because it is a derivative based approach it can be used as a direct reference to our weighting solutions. In the AIUB standard screening the first time derivative of the geometry-free linear combination is computed without any smoothing using the half difference of the previous and the next epoch, which is equivalentot the three point differentiating scheme shown in section 2.4. Comparing this method to our differentiating scheme, compare figure 6, the differences are visible, but both derivatives show similar amplitude and shape. If the absolute value of the first time derivative exceeded $2cm/s$, the observation was removed from the RINEX observations file. This introduces data gaps which are mostly responsible for the increased number of ambiguity parameters due to a very conservative setting up of new ambiguity parameters if data gaps are longer then 61 sec.. In cases, where too many observations had to be removed, the kinematic positions could not be computed anymore.

3.2 Derivative based weighting

In the derivative based weighting schemes, we tested the first, second and third time derivative. As mentioned in section 2.4 we use a combination of a Gaussian- and a Savitzky-Golay-filter. This additional effort is necessary due to noise of L_{GF}. As shown in section 2.4 already for the second time derivative using a classical three-point differentiation scheme, one would basically see noise.

After computing the numerical time derivatives, we apply empirical thresholds. These thresholds were set by checking the amplitude of the derivatives, evaluating the performance on the gravity field level, and the threshold used by (Jäggi et al., 2016). The thresholds were set to $2 \mathrm{cms}^{-1}$ for $\frac{dL_{GF}}{dt}$, $0.025 \mathrm{cm\,s}^{-2}$ for $\frac{d^2L_{GF}}{dt^2}$ and $0.00075 \mathrm{cm\,s}^{-3}$ for $\frac{d^3L_{GF}}{dt^3}$.

If the time derivative at a certain epoch exceeds the threshold, an observation specific σ of 21 (standard $\sigma + 20$)is given to the observation instead of a standard unweighted σ of 1. This kind of extreme down-weighting is used to have a similar impact on the orbit as the standard screening, but because the observations stay in the RINEX observation file and also in the resulting normal equation system, no gaps are introduced and no additional ambiguities that are weakening the orbit. In case an observation epoch was too close to a gap or a jump and no derivative could be computed, the data point was down weighted in addition assuming that the observation might be affected. The third time derivative suffers most from enlarged gaps due to non-computable derivatives and gravity field recoveries based on correspondingly generated kinematic orbits turned out to be of inferior quality. For that reason we focus on the first and second time derivative in the following sections.

For the first time derivative we set the thresold to obtain similar results as with the AIUB standard screening to have a zero-test and to gain additional insight in the difference between screening and weighting. This as intended to perform as kind of zero-test and also giving hint to the differences between screening and weighting.

3.3 ROTI based weighting

The ROTI (Rate Of TEC Index) based weighting was used by Zehentner and Mayer-Gürr (2015) for the GOCE orbit processing, where similar issues have been observed Jäggi et al. (2015). ROTI is defined as

$$ROTI = \sqrt{\frac{\langle \Delta TEC^2 \rangle - \langle \Delta TEC \rangle^2}{\Delta t^2}} \tag{3}$$

5   and is applied in a sliding window manner (Pi et al., 1997). The window size is set symmetrically with a width of $31s$. The differences to determine the ΔTEC were computed using the previous and the current epoch:

$$\Delta TEC(t_i) = TEC(t_i) - TEC(t_{i-1}) \tag{4}$$

In analogy to Sect. 3.2 the points were downweighted with a sigma of 21 if the number of data points was below a threshold of 10. For the ROTI approach, we tested two different scaling functions. First we used the scaling function applied by Zehentner

10   and Mayer-Gürr (2015) for GOCE, which reads as $\sigma = max(1, 20 \cdot ROTI)$. This approach, however, turned out not to have an impact on the Swarm Data. For our tests, we therefore modified the weighting according to

$$\sigma_{ROTI}^{AIUB} = max(1, 60 \cdot ROTI) \tag{5}$$

or alternatively as proposed for Swarm, private communication, N. Zehentner, 2017

$$\sigma_{ROTI}^{GRAZ} = exp(20 \cdot ROTI). \tag{6}$$

15   In case the ROT-Index is small, both approaches should return a σ close to 1. In case of high fluctuations, where ROTI gets large, the second weights are much larger. The first set of weights will be referred as ROTI 1, the latter as ROTI 2. As one can see in figure 7 the ROTI weights are particularly pronounced in regions where die ionosphere-free phase residuals are large. ROTI turned out to be most effective in the polar regions due to the presence of plasma density fluctuations.

3.4 Localizing the weights

20   We are aiming to reduce the impact of the artifacts induced by the equatorial ionosphere on the gravity fields and consequently improve the quality of the obtained gravity fields. Some of our derivative-based approaches led to a degradation of the gravity fields in the polar regions as will be shown in section 4.1. To avoid this degradation we are limiting our derivative based weighting to equatorial regions with a latitude between $-50°N$ and $50°N$. Due to the shape of the geomagnetic equator (which is located between roughly $\pm 13°$lattitude) and the of the equatorial ionization anomaly, which is located between

25   $-20Mlat$ and $20Mlat$ (Whalen, 2000), this covers all the equatorial ionosphere. For the ROTI approaches no such limitation was performed due to the positive effect in the polar regions.

3.5 Combination of Methods

Because the ROTI weighting is powerful at the polar regions and the derivative based weighting in the equatorial regions, we combine both methods. Because the scaling function in case of the AIUB-scaled ROTI 1 provides less extreme weights, we
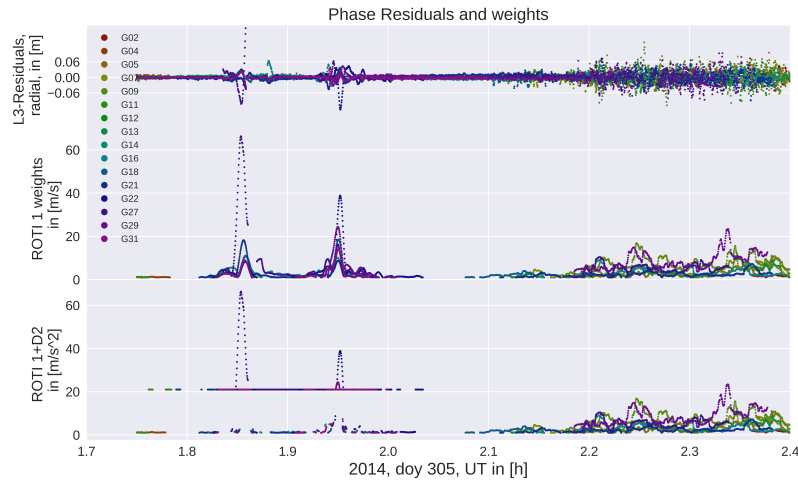
Figure 7. Ionosphere-free phase residuals (top), AIUB-ROTI sigmas (middle) and AIUB-ROTI combined with the second derivative (bottom). Around 1.9 UT there is an equatorial pass and around 2.3 UT a polar pass. The ROTI sigmas are very present at the polar region, the second derivative with a fixed sigma is more restrictive at equatorial regions.

decided to combine this one to the second derivative. This is achieved by taking the maximum of the ROTI-sigma and the second derivative based sigma in the equatorial regions, compare figure 7.

4 Evaluation

4.1 Swarm gravity field recovery

5 In order to validate our gravity field reovery results, we use the static AIUB-GRACE03S gravity field model as a reference field. Due to the ultra-precise K-Band inter-satellite measurements the GRACE gravity fields are of very high quality and essentially free from systematic ionospheric errors. In figure 8 (top left) we computed the geoid height differences between the AIUB-GRACE03S gravity field and monthly Swarm GPS only gravity fields using the un-screened and unweighted orbits. The specific month, march 2015, is heavily affected. The stripes around the geomagnetic equator are clearly visible with an
10 amplitude of around $4cm$ in geoid height when adopting a Gaussian filter radius of $500km$. In case of the gravity fields obtained using the AIUB standard screening (top, right), these two bands have virtually disappeared.

As a first step we compare the AIUB standard screening with the weighting based on the first derivative This zero test shows a similar performance as the standard AIUB screening, but especially in the pacific region it seems to add some additional artifacts. Figure 13 explains the different behavior, if we compare to the positions that were actually used for the gravity field
15 recovery. The standard screening removes almost all positions in that specific area, in contrast to the weighting, were the positions are preserved, but minor artifacts appear.

In order to remove the two bands we see, that the second derivative has a similar performance w.r.t. the AIUB standard screening. In particular also the artifact in the pacific region vanished. In contrast to the standard screening, the noise seems slightly reduced. Using the second derivative with no geographical restrictions, we see some larger fluctuations around the polar regions. For this reason we limit the second derivative based weighting to the equatorial regions.

5 In removing the two bands both ROTI approaches are not very successful, but concerning the polar regions, the ROTI based gravity fields show reduced noise. This impression is supported by the degree difference amplitudes shown in figure 9. For degrees above 25 the degree differences of both ROTI approaches are among the lowest. A different picture results, howver, gets visible if one focuses on the degree differences between degree 15 and 25. In these degrees the performance of the derivative based screening and weighting approaches clearly outperforms the ROTI solutions. These degrees are the specific

10 degrees, where the equatorial artifact is located in.

If one compares the AIUB screening to the second derivative, the AIUB screening shows a slightly better performance in the low degrees (< 10) but in most of the higher degrees the latter one shows a similar or even better performance. Because the second derivative proofed very successful in removing the artifact, and the ROTI approach is most effective in reducing the noise and improving the gravity field in polar regions, it makes sense to combine both. For this purpose we tested a combination

15 of ROTI 1 and the second derivative limited to the equator using the maximum sigma ob both approaches. The differences in the gravity field, see figure 8, still show some increased noise around the geomagnetic equator, but it is about the same level we had with the second derivative based weighting. Especially above Greenland the gravity field benefits from the ROTI weighting. Looking again to the degree difference amplitudes, the light blue line is above the lowest for almost all degrees. In total a combination seems to be most efficient and result into the best gravity fields in this comparison.

20 ## 4.2   Weighted observations

It is our ambition to remove the equatorial artifact by down-weighting as few epochs as possible. In the derivative based cases we specified a clearly defined threshold. , which allows to decide if needs to be downweighted or not.

However, the ROTI approach affects almost all epochs, even if most of the weights are small. To evaluate how many epochs are heavily down-weighted we therefore set thresholds to the ROTI derived weights, to identify which observations are assigned

25 strong weights. For representation purposes we chose two different thresholds for ROTI-based weights: $\sigma > 2$ and $\sigma > 5$.

In Figure 10 the percentage of weighted Observations is illustrated in geomagnetic coordinates. Even though the first and second derivative show a similar performance, the weights based on the first derivative seems to act more on the outer boundary of the Appleton anomaly than the weights determined by the second time derivative. Using the second derivative is therefore beneficial, if one assumes, that the spikes in the kinematic positions are aligned with the sharp peaks in plasma density and not

30 on the flanks of the anomaly, which can be seen in figure 1. Evaluating the third time derivative one can see, that a too high number of Observations gets weighted. Almost any observation around the pole is touched.

The ROTI weighting approach is, however, much more sensitive to fluctuations in the geometry-free linear combination as they occur on the poles or due to equatorial plasma bubbles, but it is not as successful in removing the equatorial artifact. If one compares the ratio of weighted observations in figure 10 for AIUB-ROTI>2 (middle left) and AIUB-ROTI>5 (bottom), the
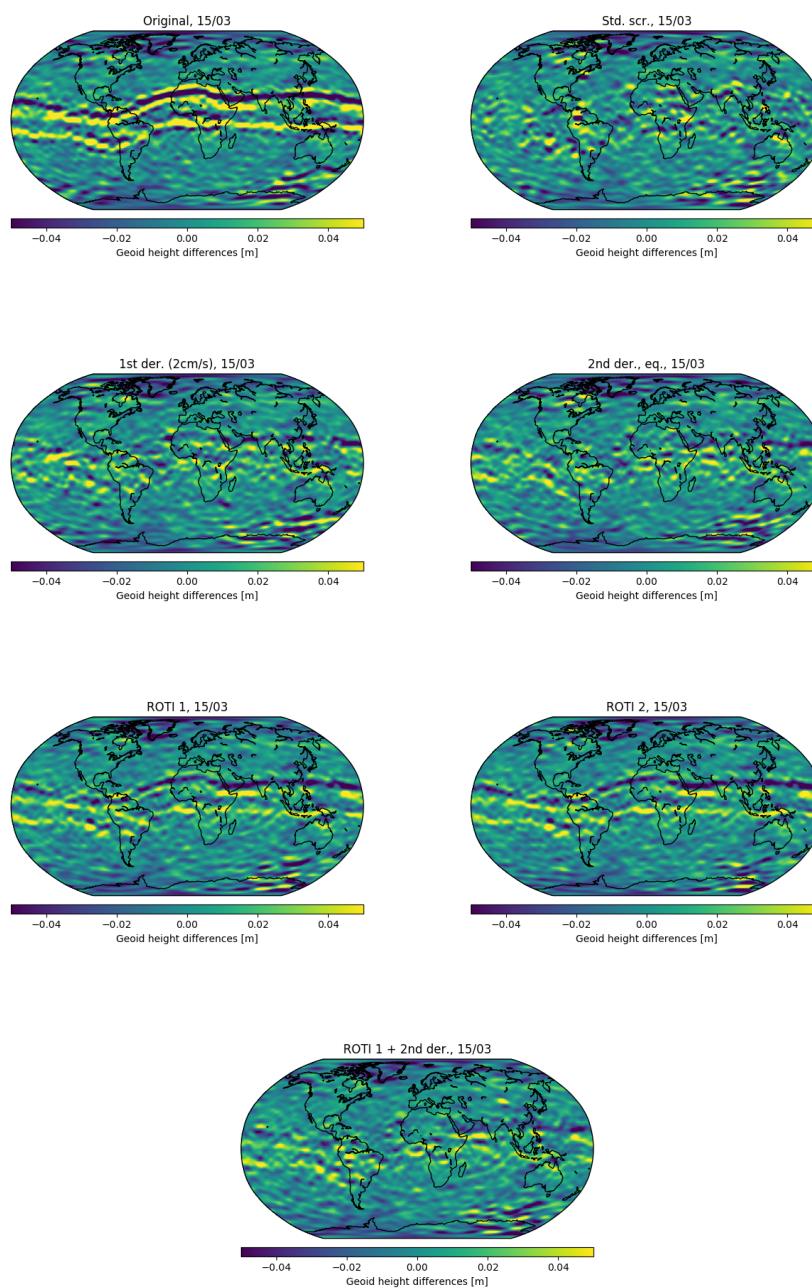
Figure 8. Differences between monthly Swarm gravity field to the AIUB-GRACE03S solution for march 2015
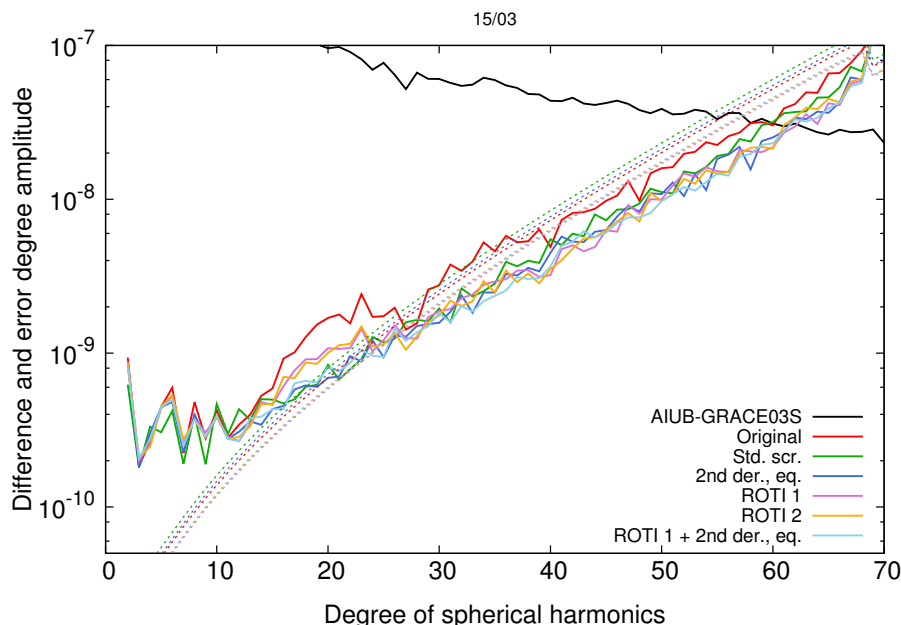
Figure 9. Difference (solid lines) and Error (dashed lines) degree Amplitude for monthly Swarm A gravity field w.r.t. AIUB-GRACE03S, march 2015

amount of weighted observations in the polar regions decreases significantly with the increased threshold. This implies that to most of the observations not very large weights are assigned. This explains why the dynamic ROTI weighting shows such a good performance around the poles. It is able to identify noisy observations and therefore reduce high frequency noise in the gravity field solutions. The ROTI information is therefore to be used as a potential descriptor of the stochastic model of the

5   GPS observations used for the positioning. Unfortunately the systematically biased positions in the equatorial regions can not reliable be identified by a high ROTI value. This may be seen in figure 10 when comparing the plots in the top row to the plot at the bottom.

Again a benefit from using the second derivative instead of the first derivative may be seen. The number of weighted/screened positions is similar too, maybe slightly smaller, but the difference and error degree amplitude is reduced, especially in the

10   higher degrees, see figure 9. Also the geoid-RMS is reduced by $1.1mm$ for March 2015, a heavily affected month, see table 1.

4.3   Orbit

Analyzing the orbits, we see that he differences between kinematic and reduced dynamic positions (see figure 11) are almost unaffected. The spikes are still present. Low frequency differences are introduced due to different empirical accelerations, caused by down-weighting systematically affected observations in the least-square fit. This may be illustrated in particular by

15   comparing the differences of the reduced dynamic orbits to the unweighted reference, see figure 12 (left). The comparison reveals low-frequency differences of up to $1cm$ amplitude. Analyzing the kinematic positions on the right-hand side, one can
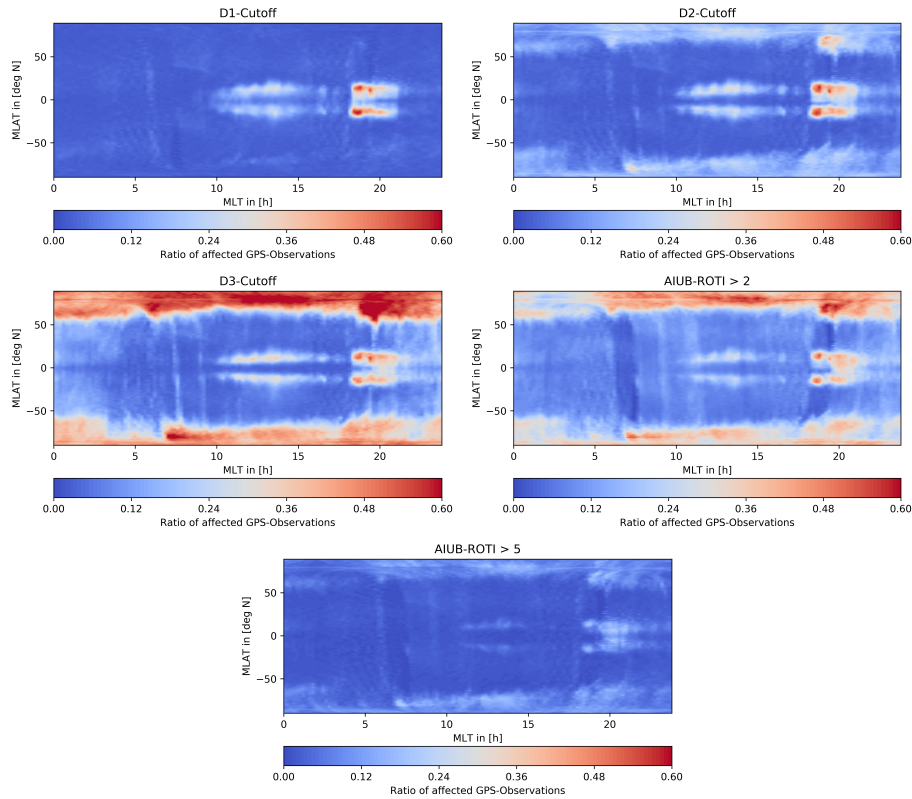
Figure 10. Ratio of weighted raw GPS measurements. Top: D1-Cutoff(left), D2-Cutoff (right), middle: D3-Cutoff (left), ROTI>2 (right), bottom: ROTI>5

see big differences around the polar regions and in the equatorial regions, too of up to $10cm$. Such large difference are, however, only visible for very few epochs. In all four cases presented the differences are spatially very localized. Considering the Graz-ROTI weighting, one can see a jump in the radial component and the along track component in the kinematic positions. This is an indicator, that the scaling function introduces too large weights. Such jumps also occur at other epochs for the Graz-ROTI, but in a few cases they also occure in other weighting strategies, when large weights are applied.

In all other cases the differences especially between the kinematic positions are very small in between the polar regions and the equatorial anomaly.

4.4 Covariances

The gravity field is not only determined by the used kinematic positions (pseudo-observations) but also by their covariance information. To demonstrate how different the weighting schemes affect the covariance information of kinematic positions, we analyze the covariances of the kinematic positions as a function of their geographic and geomagnetic locations, respectively. The information was binned ($1° lat \times 1° lon$ degree for geographic and $1° Mlat \times 0.2h MLT$) and the mean of the radial
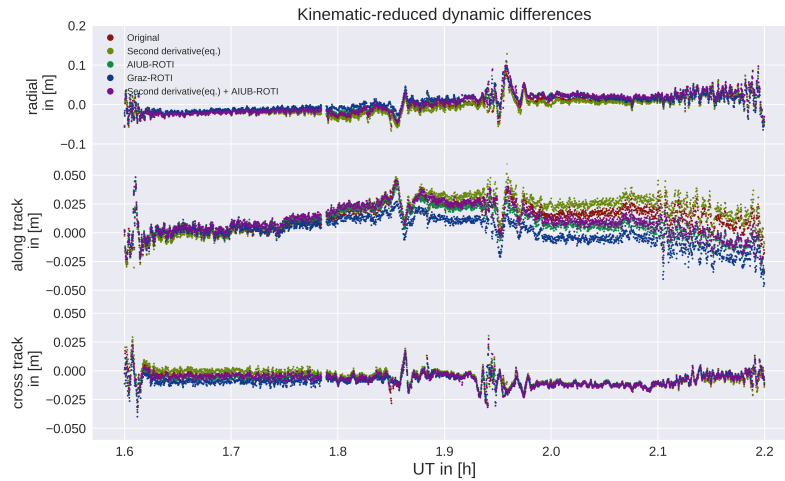
Figure 11. Kinematic minus reduced dynamic positions in radial, along- and cross-track. For both, kinematic and reduced dynamic positions, the same weighting was applied
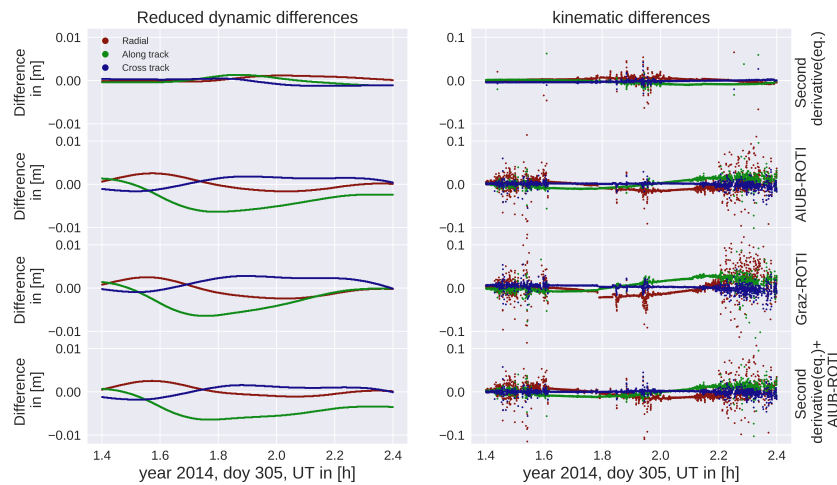
Figure 12. Differences between the unweighted positions of reduced dynamic (left) and kinematic (right) orbits. All Orbits were compared to the unweighted case.

variances, see section 2.1, was computed. For better visibility the logarithm of that mean was taken. As already mentioned, one can see that for the AIUB standard screening the covariances are a single band along the equator, compare figure 14 and 15 top, left. The positions below and above the equator don't show big covariances, but they are significantly decreased
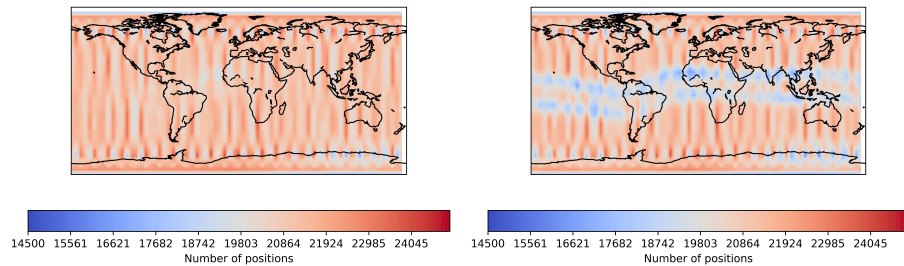
Figure 13. Absolute number of kinematic positions for the analyzed test period, un-screened (left) and with AIUB standard screening (right)

as figure 13 illustrates. Between the two peaks the geometry of the observations is weakened resulting in high variances. In the two bands too many observations are affected by the screening resulting in a significant loss of positions. For the second derivative based weighting approach, we see two bands around the geomagnetic equator, compare with figure 14 and 15 bottom right. The positions in between are of significantly better quality as the positions obtained using AIUB standard screening. As
5   mentioned for the ROTI approaches, highest variances are resulting for areas of fluctuations such as the poles and equatorial region regions around 18-22 MLT, which are well-known for equatorial plasma bubbles. This may be well recognized when plotting the covariances in geomagnetic coordinates (figure 15). Using the second derivative in addition to the ROTI (bottom right) results in higher covariances in the tow bands around the geomagnetic equator, also higher covariances in earlier LT may be recognized. This illustrates the different sensitivities of the two approaches.
10 The covariance information plays an important role for the gravity field processing (Prange et al., 2009). It is is used for weighting in the least square adjustment. If systematically biased positions have high covariance, their impact on the gravity field gets automatically reduced.

4.5   Validation

As an independent validation of the obtained orbits, we use satellite laser ranging (SLR) measurements and compute the
15 differences between the SLR-measurement and the computed distances. As Additional criteria we use the L1-phase RMS of the orbit of the GPS data, the RMS of the geoid height differences with respect to a superior solution based on ultra-precise GRACE K-Band measurements, and the (cos of latitude) weighted standard deviation above the ocean (Meyer et al., 2012), see table 1 and 2. It is interesting that we could preserve more positions in the weighted case than in the case without weighting, now being kept in the system with lower weight. The geoid RMS of the unscreened and screened soulutions is at the same
20 level as the values published in (Dahle et al., 2017). In the weighted scenarios for March 2015, the geoid RMS is reduced when using the second derivative for weighting or when combining the second derivative derived weights with the ROTI 1 derived weights. For June 2016 the second derivative derived weights lead to a small degradation of the geoid RMS. For this month we obtain the smallest geoid RMS when using ROTI derived weights. For both months the geoid RMS obtained when using the combination of the ROTI 1 derived weights and the second derivative derived weights is among the lowest. The ROTI
25 approaches again tend to reduce the noise, which may be seen in the reduction of the geoid RMS, even if the geoid RMS
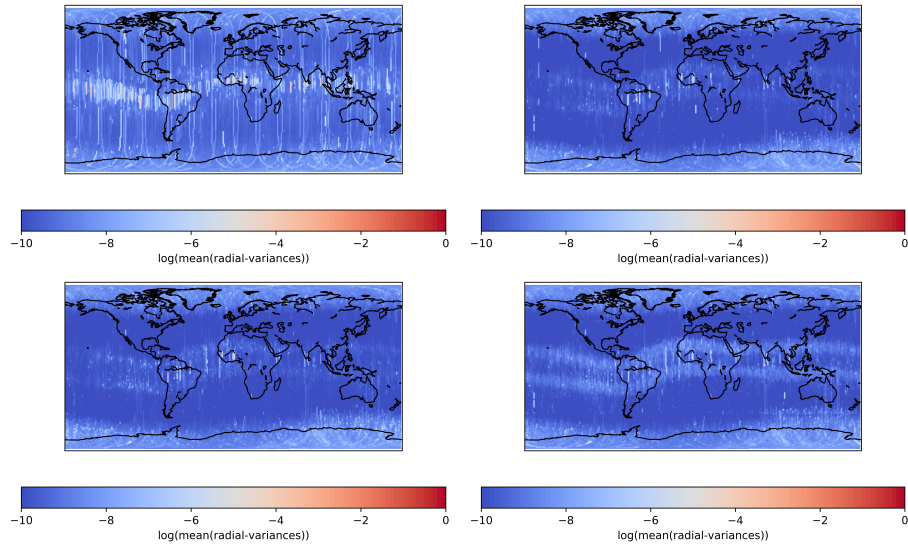
Figure 14. Kinematic Variances for the analyzed test period, global. Top: AIUB standard screening (left), AIUB-ROTI (right), bottom: GRAZ-ROTI (left), second derivative (eq.)+AIUB-ROTI (right)
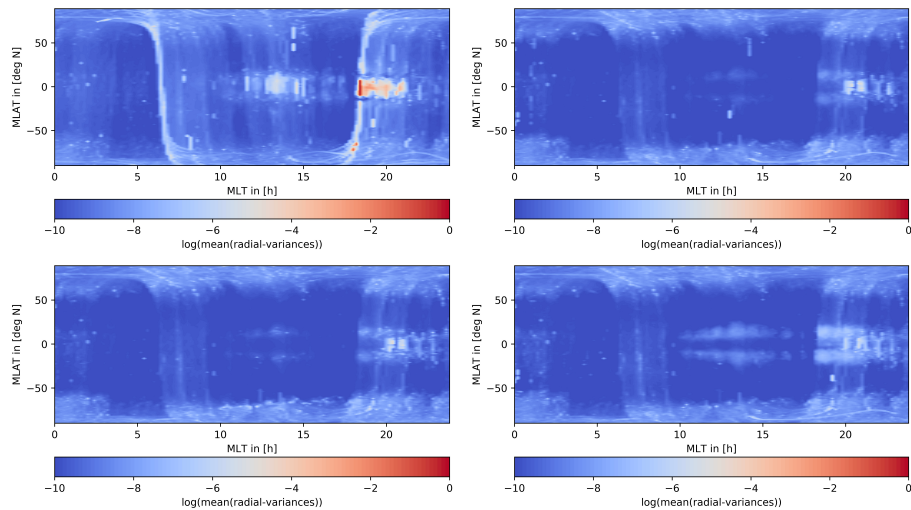
Figure 15. Kinematic Variances magnetic coordinates. Top: AIUB standard screening (left), AIUB-ROTI (right), bottom: GRAZ-ROTI (left), second derivative (eq.)+AIUB-ROTI (right)

for march 2015 is slightly bigger compared to the second derivative. This might be due to the still existing artifacts around the geomagnetic equator. The fact that this improves significantly by combining the AIUB-ROTI with the second derivative supports this assumption. The same effect is visible for the weighted standard deviation above the oceans.

The mean offsets, as well as the standard deviations are at the same level in the reduced dynamic case. In the kinematic cases

Table 1. Statistics and SLR-Residuals for Swarm A, March 2015

Scenario	# Kin. Pos.	L1 RMS [mm]	Geoid RMS [mm]	wStd Ocean [mm]	RD mean (SLR)[mm]	RD std (SLR)[mm]	KN mean (SLR)[mm]	KN std (SLR)[mm]
Original	696060	2.78	22.0	101.2	4.6	27.3	2.4	31.1
Std. scr. $dL4/dt$	636633	2.75	13.8	63.7	3.7	26.9	0.7	31.4
Wgt. d^2L4/dt^2, eq.	693648	2.64	12.9	62.1	4.6	27.3	1.9	32.5
Wgt. ROTI 1	700503	2.18	14.3	64.5	4.9	26.5	1.0	28.8
Wgt. ROTI 2	700155	2.11	14.1	61.7	5.0	25.8	0.9	28.7
Wgt. ROTI 1 + 2nd der.	700569	2.14	12.5	55.3	5.0	26.0	0.6	29.3

Table 2. Statistics and SLR-Residuals for Swarm A, June 2016

Scenario	# Kin. Pos.	L1 RMS [mm]	Geoid RMS [mm]	wStd Ocean [mm]	RD mean (SLR)[mm]	RD std (SLR)[mm]	KN mean (SLR)[mm]	KN std (SLR)[mm]
Original	783996	2.03	8.6	45.7	3.3	14.0	1.7	16.4
Std. scr. $dL4/dt$	783153	2.01	9.1	47.0	3.2	14.2	1.7	16.6
Wgt. d^2L4/dt^2, eq.	783714	2.01	8.9	46.9	3.3	14.0	1.7	16.4
Wgt. ROTI 1	784182	1.70	7.3	37.9	3.4	14.1	1.4	16.5
Wgt. ROTI 2	784209	1.64	7.4	39.7	3.4	14.2	1.4	16.4
Wgt. ROTI 1 + 2nd der.	784128	1.69	7.4	38.9	3.3	14.2	1.3	16.7

the mean and SLR standard deviations show a slight improvement if the ROTI approach is used.

In June 2016 the validation improves, but the orbits in June 2016 are not that much affected by the ionospheric activity. This is due to the less critical local times and a reduced solar Flux index, which indicates less ionospheric activity, compare with figure 10 and table 4. But even in that case the ROTI approaches seem to be capable to improve the mean of the SLR residuals for the kinematic positions.

4.6 Weighted observations and $F10.7$-Index

As shown by Jäggi et al. (2016) the amount of screened or in our case weighted observations depends on the ionospheric activity. (Jäggi et al., 2016) used the TEC content to demonstrate this. For our study we compare the number of weighted observation to the $F10.7$-Index as well as the Kp-Index. The first one is an indicator for the ionization, whereas the second is an indicator for the geomagnetic activity. As shown by Stolle et al. (2006), the probability of an equatorial plasma bubble is positive correlated to the $F10.7$-Index. Equatorial plasma bubbles usually occur, when there is a high activity in the ionosphere. Previous studies connect bubbles to a strong vertical pre reversal enhancement, fast changes in plasma density, an unstable E-F boundary, and strong gradients (Whalen (2000), **?**,Stolle et al. (2006)). This is of course harmful to the quality of GPS-data as
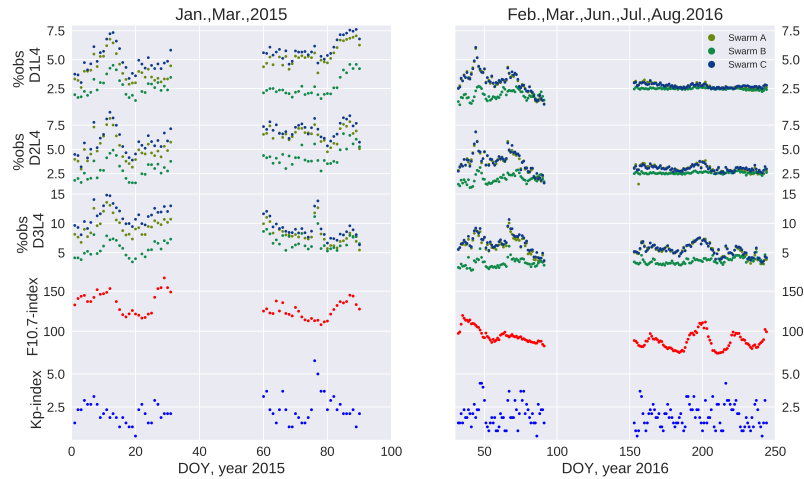
Figure 16. Percentage of screened position in comparison to the $F10.7$- and Kp-Indexes

one can see in figure 3 (left), where especially the bubble region shows high variances. So we expect a correlation between the $F10.7$-Index and the number of weighted observations.

Secondly the Kp-Index represents the disturbances in the geomagnetic field. Because the motion of ionospheric plasma is connected to the magnetic field (Kelley, 1989), disturbances in the magnetic field may result again in errors in kinematic posi-

5   tioning. So we expect again a high number of affected observations under storm conditions. These comparisons are illustrated in figure 16. To avoid contamination due to the polar regions, we limit all three data sets to the equatorial regions (lat$< 50°$). The largest daily averaged Kp-Index in our Time series is 6 on day 15076 (03/17/2015). On this day, there was a severe magnetic storm (class G4) with Kp up to $8-$. Especially in the second and third time derivative based weighting one can see a clear increase in the relative number of affected epochs. Most probably this is related to increased ionospheric fluctuations as

10   they occur in storm conditions. In total the percentage of weighted observations shows a similar behavior as the $F10.7$-Index. Some differences can be explained by the local time dependence. In total, as one can see in table 3 that the correlation between the percentage of weighted observations and the $F10.7$-Index is quite strong (above 0.7) for Swarm A and Swarm C, but a lot weaker for Swarm B. The reason might be the higher altitude of Swarm B which leads to less free electrons and weaker gradients in the ray paths to the GPS-satellites. In addition, Swarm B passes on different local times. For march 2015 the local

15   times are comparable, resulting in a very similar behavior (see fig. 16). Toward the last months (July and August 2016) the local time of Swarm B is significant different from the critical regions ($18LT - 02LT$), but in the same months Swarm A and Swarm C are inside the critical local times. Here we can clearly see the peak of the $F10.7$-Index around day 200 in the percentage of weighted observations for Swarm A and Swarm C but nothing is visible for Swarm B.

Table 3. Correlation coefficient between the relative number of weighted observations and the $F10.7$-index

Method	D1 (eq.)	D2 (eq.)	D3 (eq.)
Swarm A	0.7025	0.7313	0.7564
Swarm B	0.3005	0.46400	0.6766
Swarm C	0.7925	0.7914	0.8219

Table 4. Local Time at middle of month

Month	Jan.'15	Mar.'15	Feb.'16	Mar.'16,	Jun.'16	Jul.'16	Aug.'16
Swarm A, C	$\sim 1LT, 13LT$	$\sim 8LT, 20LT$	$\sim 2LT, 14LT$	$\sim 11LT, 23LT$	$\sim 3LT, 15LT$	$\sim 0LT, 12LT$	$\sim 9LT, 21LT$
Swarm B	$\sim 2.5LT, 14.5LT$	$\sim 9LT, 21LT$	$\sim 5LT, 17LT$	$\sim 2LT, 14LT$	$\sim 6LT, 18LT$	$\sim 3LT, 15LT$	$\sim 0LT, 12LT$

5   Conclusions

We showed that spikes in the kinematic positioning, as they occur in the obit processing of the Swarm Mission, are associated to sharp peaks in the plasma density. Furthermore, we showed that these spikes have large phase residuals and can be identified using time derivatives of the geometry-free linear combination. Based on these time derivatives we developed weighting criteria and used already existing techniques such as the ROTI approach and the AIUB standard screening. We found that the second derivative based weighting located around the equator is very efficient in removing the artifact around the geomagnetic equator. The ROTI approach improved the gravity fields in the polar regions. Eventually we evaluated the different screening approaches and combined them to an even more effective approach. The improvement of the orbits is visible in the gravity fields as well as in the SLR residuals. How different the weighting strategies apply to the observations is also visible in the covariance information of the kinematic positions. In turn this covariance information is essential to improve the gravity field solutions. The number of weighted observations, especially in the derivative based cases seems to correlate to the $F10.7$-Index representing the ionospheric activity, which is consistent to previous studies (Jäggi et al. (2016) and Xiong et al. (2016)).

Competing interests. The authors declare that they have no conflict of interest

References

Bock, H., Jäggi, A., Beutler, G., and Meyer, U.: GOCE: precise orbit determination for the entire mission, Journal of Geodesy, 88, 1047–1060, https://doi.org/10.1007/s00190-014-0742-8, https://doi.org/10.1007/s00190-014-0742-8, 2014.

Dach, R., Lutz, S., Walser, P., and (Eds), P. F.: Bernese GNSS Software Version 5.2 User manual, Astronomical Institute, University of Bern,
5 Bern Open Publishing, 2015.

Dahle, C., Arnold, D., and Jäggi, A.: Impact of tracking loop settings of the Swarm GPS receiver on gravity field recovery, Advances in Space Research, 59, 2843 – 2854, https://doi.org/10.1016/j.asr.2017.03.003, http://www.sciencedirect.com/science/article/pii/S027311771730176X, 2017.

Jäggi, A., Bock, H., Meyer, U., Beutler, G., and van den IJssel, J.: GOCE: assessment of GPS-only gravity field determination, Journal of
10 Geodesy, 89, 33–48, https://doi.org/10.1007/s00190-014-0759-z, https://doi.org/10.1007/s00190-014-0759-z, 2015.

Jäggi, A., Bock, H., Prange, L., Meyer, U., and Beutler, G.: GPS-only gravity field recovery with GOCE, CHAMP, and GRACE, Advances in Space Research, 47, 1020 – 1028, https://doi.org/10.1016/j.asr.2010.11.008, http://www.sciencedirect.com/science/article/pii/S0273117710007350, 2011a.

Jäggi, A., Prange, L., and Hugentobler, U.: Impact of covariance information of kinematic positions on orbit reconstruction and gravity field
15 recovery, Advances in Space Research, 47, 1472 – 1479, https://doi.org/10.1016/j.asr.2010.12.009, http://www.sciencedirect.com/science/article/pii/S0273117710007969, 2011b.

Jäggi, A., Dahle, C., Arnold, D., Bock, H., Meyer, U., Beutler, G., and van den IJssel, J.: Swarm kinematic orbits and gravity fields from 18months of GPS data, Advances in Space Research, 57, 218 – 233, https://doi.org/10.1016/j.asr.2015.10.035, http://www.sciencedirect.com/science/article/pii/S0273117715007541, 2016.

20 Kelley, M. C.: Chapter 2 - Fundamentals of Ionospheric Plasma Dynamics, in: The Earth's Ionosphere, edited by Kelley, M. C., pp. 23 – 63, Academic Press, https://doi.org/10.1016/B978-0-12-404013-7.50007-1, http://www.sciencedirect.com/science/article/pii/B9780124040137500071, 1989.

Lück, C., Kusche, J., Rietbroek, R., and Löcher, A.: Time-variable gravity fields and ocean mass change from 37 months of kinematic Swarm orbits, Solid Earth, 9, 323–339, https://doi.org/10.5194/se-9-323-2018, https://www.solid-earth.net/9/323/2018/, 2018.

25 Meyer, U., Jäggi, A., and Beutler, G.: Monthly gravity field solutions based on GRACE observations generated with the Celestial Mechanics Approach, Earth and Planetary Science Letters, 345-348, 72 – 80, https://doi.org/10.1016/j.epsl.2012.06.026, http://www.sciencedirect.com/science/article/pii/S0012821X1200310X, 2012.

Pi, X., Mannucci, A. J., Lindqwister, U. J., and Ho, C. M.: Monitoring of global ionospheric irregularities using the Worldwide GPS Network, Geophysical Research Letters, 24, 2283–2286, https://doi.org/10.1029/97GL02273, 1997.

30 Prange, L., Jäggi, A., Beutler, G., Dach, R., and Mervart, L.: Gravity Field Determination at the AIUB – The Celestial Mechanics Approach, in: Observing our Changing Earth, edited by Sideris, M. G., pp. 353–362, Springer Berlin Heidelberg, Berlin, Heidelberg, 2009.

Stolle, C., Lühr, H., Rother, M., and Balasis, G.: Magnetic signatures of equatorial spread F as observed by the CHAMP satellite, Journal of Geophysical Research: Space Physics, 111, https://doi.org/10.1029/2005JA011184, https://agupubs.onlinelibrary.wiley.com/doi/abs/10.1029/2005JA011184, 2006.

35 Whalen, J. A.: An equatorial bubble: Its evolution observed in relation to bottomside spread F and to the Appleton anomaly, Journal of Geophysical Research: Space Physics, 105, 5303–5315, https://doi.org/10.1029/1999JA900441, https://agupubs.onlinelibrary.wiley.com/doi/abs/10.1029/1999JA900441, 2000.

Xiong, C., Stolle, C., and Lühr, H.: The Swarm satellite loss of GPS signal and its relation to ionospheric plasma irregularities, Space Weather, 14, 563–577, https://doi.org/10.1002/2016SW001439, https://agupubs.onlinelibrary.wiley.com/doi/abs/10.1002/2016SW001439, 2016.

Zehentner, N. and Mayer-Gürr, T.: Mitigation of ionospheric scintillation effects in kinematic LEO precise orbit determination, EGU General Assembly 2015, 2015.